www.elsevier.com/locate/ijmecsci

Vibration analysis of cracked FGM plates using higher-order shear deformation theory and extended isogeometric approach

Loc V. Tran, Hung Anh Ly, M. Abdel Wahab, H. Nguyen-Xuan

PII: S0020-7403(15)00079-X
DOI: http://dx.doi.org/10.1016/j.ijmecsci.2015.03.003
Reference: MS2944

To appear in: *International Journal of Mechanical Sciences*

Received date: 1 March 2014
Revised date: 19 January 2015
Accepted date: 5 March 2015

Cite this article as: Loc V. Tran, Hung Anh Ly, M. Abdel Wahab, H. Nguyen-Xuan, Vibration analysis of cracked FGM plates using higher-order shear deformation theory and extended isogeometric approach, *International Journal of Mechanical Sciences*, http://dx.doi.org/10.1016/j.ijmecsci.2015.03.003

Vibration analysis of cracked FGM plates using higher-order shear deformation theory and extended isogeometric approach

Loc V. Tran[1], **Hung Anh Ly**[2], **M. Abdel Wahab**[1], **H. Nguyen-Xuan**[3,4*]

[1]Department of Mechanical Construction and Production, Faculty of Engineering and Architecture, Ghent University, 9000, Ghent – Belgium

[2]Department of Aerospace Engineering, Faculty of Transportation Engineering, Ho Chi Minh City University of Technology, VNU-HCMC, 268 Ly Thuong Kiet Street, Ho Chi Minh, Vietnam

[3]Department of Computational Engineering, Vietnamese – German University, Binh Duong New City, Vietnam

[4]Department of Architectural Engineering, Sejong University, Seoul, South Korea

Abstract

A novel and effective formulation that combines the eXtended IsoGeometric Approach (XIGA) and higher-order shear deformation theory (HSDT) is proposed to study the free vibration of cracked functionally graded material (FGM) plates. Herein, the general HSDT model with five unknown variables per node is applied for calculating the stiffness matrix without needing shear correction factor (SCF). In order to model the discontinuous and singular phenomena in the cracked plates, IsoGeometric Analysis (IGA) utilizing the Non-Uniform Rational B-Spline (NURBS) functions is incorporated with enrichment functions through the partition of unity method. NURBS basis functions with their inherent arbitrary high order smoothness permit the C^1 requirement of the HSDT model. The material properties of the FGM plates vary continuously through the plate thickness according to an exponent function. The effects of gradient index, crack length, crack location, length to thickness on the natural frequencies and mode shapes of simply supported and clamped FGM plate are studied. Numerical examples are provided to demonstrate the performance of the proposed method. The obtained results are in close comparison with other published solutions in the literature.

* Corresponding author. *Email address*: hung.nx@vgu.edu.vn (H. Nguyen-Xuan)

Keywords Functionally Graded Material, Non-Uniform Rational B-Spline, Higher-order Shear Deformation Theory, Vibration, Cracked Plate

1. Introduction

Functionally Graded Materials (FGMs) [1-3] have been investigated and developed during past three decades. FGM is often a mixture of two distinct material phases: e.g. ceramic and metal with the variation of the volume fraction according to power law through the thickness. As a result, FGMs are enabled to inherit the best properties of the components, e.g. low thermal conductivity, high thermal resistance by ceramic and ductility, durability of metal. They are therefore more suitable to use in aerospace structure applications and nuclear plants, etc.

In order to use FGMs efficiently, a clear understanding of their behaviors such as deformable characteristic, stress distribution, natural frequency and critical buckling load under various conditions is required. Hence, investigation on property of FGM structure has been addressed since long time. For instance, Reddy [4] proposed an analytical formulation based on a Navier's approach using the third-order shear deformation theory and the von Kármán-type geometric non-linearity. Vel and Battra [5,6] introduced an exact formulation based on the form of a power series for thermo-elastic deformations and vibration of rectangular FGM plates. Yang and Shen [7] have analyzed the dynamic response of thin FGM plates subjected to impulsive loads. Cinefra et al. [8] investigated the response of FGM shell structure under mechanical load. Nguyen et al. [9-12] studied the behaviors of FGM plates using numerical methods. Ferreira et al. [13,14] performed static and dynamic analysis of FGM plate based on higher-order shear and normal deformable plate theory using the meshless local Petrov–Galerkin method. Tran et al. [15] studied the thermal buckling of FGM plate based on third-order shear deformation theory.

From the literature, these works are carried out for designing the FGM plate structures without the presences of cracks or flaws. However, during manufacturing the FGM or general plate structures may have some flaws or defects. In service, the cracks can be generated and grown from the defects under a cyclic loading. It is known that the cracks affect on the dynamic response and stability characteristics of the plate structures. They cause a reduction of the load carrying capacity of the plate

structures. Therefore, various researches on dynamic behavior of cracked plates become more necessary for engineers and designers.

Vibration of cracked plates was early studied in 1967 by Lynn and Kumbasar [16] using Green's function for approximating the transverse displacements. Stahl and Keer [17] used the Levy-Nadai approach and the homogeneous Fredholm integral equations of the second kind to deal with the free vibration analysis of the cracked rectangular plates. Hirano and Okazaki [19] utilized the Levy solution to investigate eigenvalue problems of the cracked rectangular plates with two opposite edges simply supported. Qian [20] applied a finite element method (FEM) to the free vibration analysis of the square thin plates. Krawczuk [21] presented a finite element model to evaluate the influence of the crack location and its length on the amplitude of the natural frequencies. Su et al. [22] further extended FEM to the free vibration analysis of thin plates with arbitrary boundary conditions. Yuan and Dickinson [23] introduced the artificial springs at the interconnecting boundaries in the Reyleigh-Ritz method to analyze the flexural vibration of rectangular plates. Lee and Lim [24] studied the natural frequency of rectangular plates with the central crack by considering transverse shear deformation and rotary inertia. Also, Liew et al. [25] used domain decomposition method to devise the plate domain into the numerous subdomains around the crack location. Recently, Huang and Leissa [26] utilized the famous Ritz method with special displacement functions to take into account the stress singularity near the crack tips.

Almost researches focused on considering thin homogenous plates based on the classical plate theory (CPT). However, to produce accurately the natural frequency of moderate and thick anisotropic plates the transverse shear deformation needs to be taken into account. According to author's knowledge, there are a few publications in the free vibration analysis of cracked plates regarding the transverse shear deformation. Bachene et al. [27] ultilized the extended finite element method (XFEM) to analyze the free vibration of cracked rectangular plates based on the first-order shear deformation theory (FSDT). However, they only used Heaviside function for discontinuous enrichment and ignored the asymptotic functions in approximation of singular field near the crack tips. Natarajan et al. [28] extended XFEM to the dynamic analysis of FGM plates. FSDT is simple to implement into the existing codes and is applicable to both thick and thin FGM plates. However, the accuracy of solutions will be strongly dependent on the shear correction factors (SCF) of which their values are quite dispersed through each problem, e.g. SCF is equal to 5/6 in Ref.[29], $\pi^2/12$ in

Ref.[30] or a complicated function derived from equilibrium conditions [31]. Huang et al. [32] used the Ritz method and the Reddy's third-order shear deformation theory (TSDT) to obtain the free vibration solution of FGM thick plates with side cracks. Yang et al. [33] studied the nonlinear dynamic response of the cracked FGM plates based on TSDT using the Galerkin method. Recently, Huang et al. [34] employed three-dimensional elasticity theory to study the free vibration of cracked rectangular FGM plates.

In this paper, we present the higher-order shear deformation theory (HSDT) for modeling cracked FGM plates. It is worth mentioning that this model requires C^1-continuity of the generalized displacements leading to the second-order derivative of the stiffness formulation which causes some obstacles in standard C^0 finite formulations. Fortunately, it is shown that such a C^1-HSDT formulation can be easily achieved using a NURBS-based isogeometric approach [35, 36]. In addition, to capture the discontinuous phenomenon in the cracked FGM plates, the enrichment functions through the partition of unity method (PUM) originated by Belytschko and Black [37] are incorporated with NURBS basic functions to create a novel method as so-called eXtended Isogeometric Analysis (XIGA). XIGA has then been applied to stationary and propagating cracks in 2D [38], plastic collapse load analysis of cracked plane structures [39] and cracked plate/shell structures [40]. Herein, our study focuses on investigating the vibration of the cracked FGM plate with an initial crack emanating from an edge or centrally located. Several numerical examples are given to show the performance of the proposed method and results obtained are compared to other published methods in the literature.

The paper is outlined as follows. The governing equation for FGM plate based on HSDT model is introduced the next section. In section 3, an incorporated method between the enrichment functions through PUM and IGA–based NURBS function are used to simulate the cracked FGM plates. Numerical results and discussions are provided in section 4. Finally, the article is closed with some concluding remarks.

2. Governing equations for functionally graded plates

2.1. Functionally graded material

Functionally graded material is a composite material which is created by mixing two distinct material phases. Two mixed materials are often ceramic at the top and metal at the bottom as shown in Figure

1. In our work, two homogenous models have been used to estimate the effective properties of the FGM include the rule of mixture [4] and the Mori-Tanaka technique [41]. Herein, the volume fraction of the ceramic and metal phase is described by the following power-law exponent function

$$V_c(z) = \left(\frac{1}{2} + \frac{z}{h}\right)^n , \; V_m = 1 - V_c \tag{1}$$

where subscripts *m* and *c* refer to the metal and ceramic constituents, respectively. Eq. (1) implies that the volume fraction varies through the thickness based on the power index *n*.

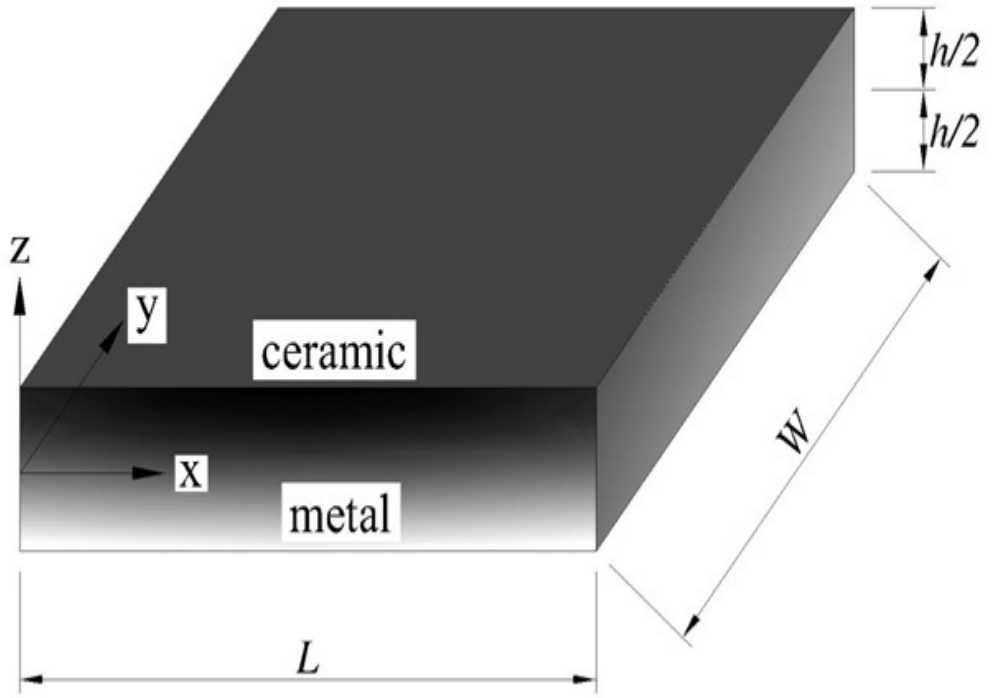

Figure 1: The functionally graded plate model.

The effective material properties according to the rule of mixture are given by

$$P_e = P_c V_c + P_m V_m \tag{2}$$

where P_c and P_m denote the material properties of the ceramic and the metal, respectively, including the Young's modulus *E*, Poisson's ratio ν and the density ρ.

However, the rule of mixture does not consider the interactions among the constituents [42]. So, the Mori-Tanaka technique [41] is then used to take into account these interactions with the effective bulk and shear modulus defined using the following:

$$\begin{aligned}\frac{K_e - K_m}{K_c - K_m} &= \frac{V_c}{1 + V_m \frac{K_c - K_m}{K_m + 4/3\mu_m}} \\ \frac{\mu_e - \mu_m}{\mu_c - \mu_m} &= \frac{V_c}{1 + V_m \frac{\mu_c - \mu_m}{\mu_m + f_1}}\end{aligned} \tag{3}$$

where $f_1 = \dfrac{\mu_m(9K_m + 8\mu_m)}{6(K_m + 2\mu_m)}$. And the effective values of Young's modulus E and Poisson's ratio ν are given by

$$E_e = \frac{9K_e\mu_e}{3K_e + \mu_e}, \qquad \nu_e = \frac{3K_e - 2\mu_e}{2(3K_e + \mu_e)} \tag{4}$$

Figure 2 illustrates comparison of the effective Young's modulus of Al/ZrO_2 FGM plate calculated by the rule of mixture and the Mori-Tanaka scheme via the power index *n*. Note that with homogeneous material, the two models produce the same values. For inhomogeneous material, the effective property through the thickness of the former is higher than that of latter. Moreover, increasing in power index *n* leads to decrement of the material property due to the rise of metallic volume fraction.

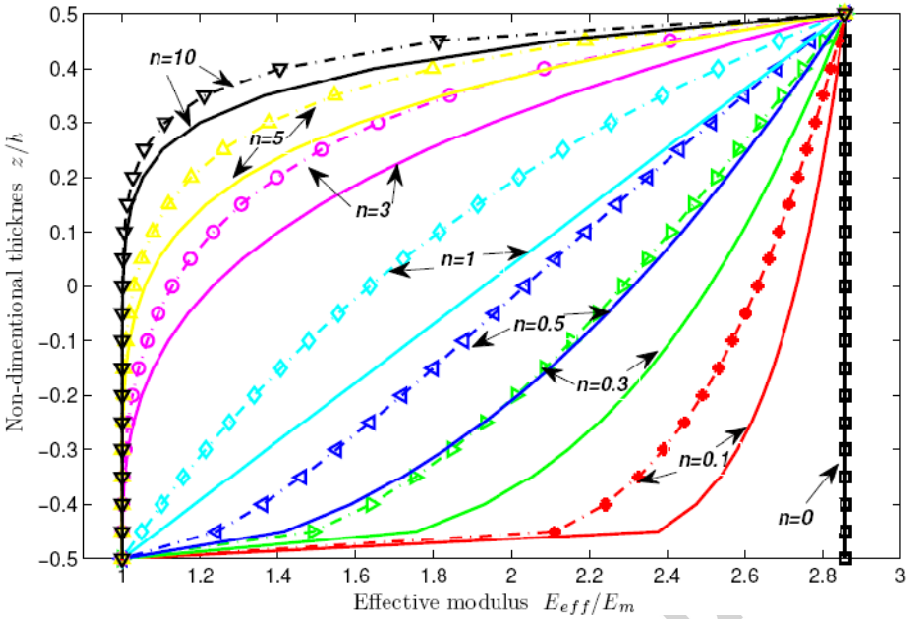

Figure 2. The effective modulus of an FGM plate computed by the rule of mixture (in solid line) and the Mori-Tanaka (in dash dot line).

2.2. General plate theory

To consider the effect of shear deformation directly, the generalized five-parameter displacement field based on higher-order shear deformation theory is defined as

$$\mathbf{u} = \mathbf{u}_1 + z\mathbf{u}_2 + f(z)\mathbf{u}_3 \tag{5}$$

where $\mathbf{u}_1 = \{u_0 \; v_0 \; w\}^T$ is the axial displacement , $\mathbf{u}_2 = -\{w_{,x} \; w_{,y} \; 0\}^T$ and $\mathbf{u}_3 = \{\beta_x \; \beta_y \; 0\}^T$ are the rotations in the x, y and z axes, respectively. $f(z)$ is the so-called distributed function which is chosen to satisfy the tangential zero value at the plate surfaces, i.e. $f'(\pm h/2) = 0$. Based on this condition, various distributed functions $f(z)$ have been devised: third-order polynomials by Reddy [43], exponential function by Karama [44], sinusoidal function by Arya [45], fifth-order polynomial by Nguyen [46] and inverse tangent functions by Thai [47] as shown in Figure 3.

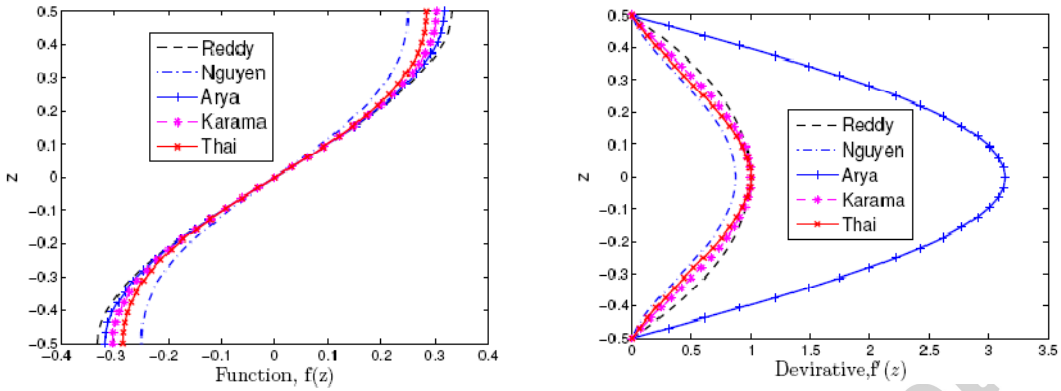

Figure 3. The shape functions and their derivative through the plate thickness.

In this work, we consider the third-order shear deformation theory (TSDT) [43] because of simplicity by setting $f(z)=z-\frac{4}{3h^2}z^3$. Of course, our current work is also available for any higher-order shear deformation theories. Moreover, by setting $f(z)=z$ and substituting $\phi_{\mathbf{x}}=-w_{,\mathbf{x}}+\beta_{\mathbf{x}}$ in Eq.(5), the first order shear deformation theory (FSDT) is obtained as

$$\begin{aligned} u(x,y,z) &= u_0+z\phi_x \\ v(x,y,z) &= v_0+z\phi_y \\ w(x,y,z) &= w \end{aligned} \tag{6}$$

As known, FSDT model requires a shear correction factor (SCF) to rectify the unrealistic shear strain energy part. In this study, SCF is fixed at 5/6.

The strains of the mid-surface deformation are derived from Eq. (5) as

$$\begin{Bmatrix} \boldsymbol{\varepsilon} \\ \boldsymbol{\gamma} \end{Bmatrix} = \begin{Bmatrix} \boldsymbol{\varepsilon}_0+z\boldsymbol{\kappa}_1+f(z)\boldsymbol{\kappa}_2 \\ f'(z)\boldsymbol{\beta} \end{Bmatrix} \tag{7}$$

where

$$\boldsymbol{\varepsilon}_0=\begin{bmatrix} u_{0,x} \\ v_{0,y} \\ u_{0,y}+v_{0,x} \end{bmatrix},\quad \boldsymbol{\kappa}_1=-\begin{bmatrix} w_{,xx} \\ w_{,yy} \\ 2w_{,xy} \end{bmatrix},\quad \boldsymbol{\kappa}_2=\begin{bmatrix} \beta_{x,x} \\ \beta_{y,y} \\ \beta_{x,y}+\beta_{y,x} \end{bmatrix},\quad \boldsymbol{\beta}=\begin{bmatrix} \beta_x \\ \beta_y \end{bmatrix} \tag{8}$$

As observed from Eq.(7), the shear stresses vanish at the top and bottom surfaces of plate.

Using the Hamilton principle, the weak form for free vibration analysis of a FGM plate can be expressed as:

$$\int_\Omega \delta\boldsymbol{\varepsilon}^T \mathbf{D}^b \boldsymbol{\varepsilon} \mathrm{d}\Omega + \int_\Omega \delta\boldsymbol{\gamma}^T \mathbf{D}^s \boldsymbol{\gamma} \mathrm{d}\Omega = \int_\Omega \delta\tilde{\mathbf{u}}^T \mathbf{m} \ddot{\tilde{\mathbf{u}}} \mathrm{d}\Omega \tag{9}$$

where

$$\mathbf{D}^b = \begin{bmatrix} \mathbf{A} & \mathbf{B} & \mathbf{E} \\ \mathbf{B} & \mathbf{D} & \mathbf{F} \\ \mathbf{E} & \mathbf{F} & \mathbf{H} \end{bmatrix} \tag{10}$$

in which

$$\begin{aligned} A_{ij}, B_{ij}, D_{ij}, E_{ij}, F_{ij}, H_{ij} &= \int_{-h/2}^{h/2} (1, z, z^2, f(z), zf(z), f^2(z)) Q_{ij} \mathrm{d}z \\ D_{ij}^s &= \int_{-h/2}^{h/2} \left[f'(z) \right]^2 G_{ij} \mathrm{d}z \end{aligned} \tag{11}$$

the material matrices are given as

$$\mathbf{Q} = \frac{E_e}{1-\nu_e^2} \begin{bmatrix} 1 & \nu_e & 0 \\ \nu_e & 1 & 0 \\ 0 & 0 & (1-\nu_e)/2 \end{bmatrix}, \quad \mathbf{G} = \frac{E_e}{2(1+\nu_e)} \begin{bmatrix} 1 & 0 \\ 0 & 1 \end{bmatrix} \tag{12}$$

Herein, the mass matrix **m** is calculated according to consistent form as follow

$$\mathbf{m} = \begin{bmatrix} I_1 & I_2 & I_4 \\ I_2 & I_3 & I_5 \\ I_4 & I_5 & I_6 \end{bmatrix} \text{ with } I_i = \int_{-h/2}^{h/2} \rho_e \left(1, z, z^2, f(z), zf(z), \left(f(z) \right)^2 \right) \mathrm{d}z \tag{13}$$

and

$$\tilde{\mathbf{u}} = \{ \mathbf{u}_1 \ \ \mathbf{u}_2 \ \ \mathbf{u}_3 \}^T \tag{14}$$

3. An extended isogeometric cracked plate formulation

3.1. B-Spline/NURBS basic functions

Let's define an open knot vector $\Xi = \{\xi_1, \xi_2, ..., \xi_{n+p+1}\}$ with a sequence of knot value $\xi_i \in \mathbb{R}$, $i = 1,...n+p$. A B-spline basis function is C^{∞} continuous inside a knot span and C^{p-1} continuous at a single knot. Therefore, as $p \geq 2$ the present approach always satisfies C^1 requirement in approximate formulations of HSDT.

The B-spline basis functions $N_{i,p}(\xi)$ are defined by the following recursion formula

$$N_{i,p}(\xi) = \frac{\xi - \xi_i}{\xi_{i+p} - \xi_i} N_{i,p-1}(\xi) + \frac{\xi_{i+p+1} - \xi}{\xi_{i+p+1} - \xi_{i+1}} N_{i+1,p-1}(\xi)$$
$$\text{as } p = 0,\ N_{i,0}(\xi) = \begin{cases} 1 & \text{if} \quad \xi_i \leq \xi < \xi_{i+1} \\ 0 & \text{otherwise} \end{cases} \tag{15}$$

By the tensor product of basis functions in two parametric dimensions ξ and η with two knot vectors $\Xi = \{\xi_1, \xi_2, ..., \xi_{n+p+1}\}$ and $\mathbf{H} = \{\eta_1, \eta_2, ..., \eta_{m+q+1}\}$, the two-dimensional B-spline basis functions are obtained by

$$N_A(\xi, \eta) = N_{i,p}(\xi) M_{j,q}(\eta) \tag{16}$$

Figure 4 illustrates the set of one-dimensional and two-dimensional B-spline basis functions according to open uniform knot vector $\Xi = \{0, 0, 0, 0, 0.5, 1, 1, 1, 1\}$.

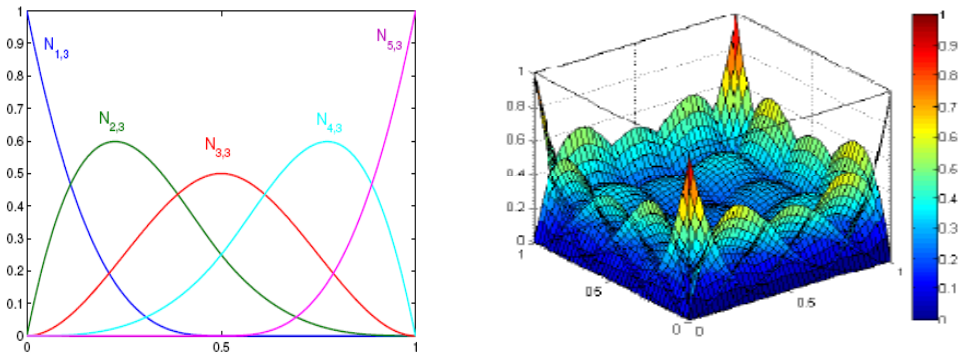

Figure 4. 1D and 2D B-spline basis functions.

To model exactly some curved geometries (e.g. circles, cylinders, spheres, etc.) the Non-Uniform Rational B-Splines (NURBS) functions are employed. Herein, a weight value ζ_A [35] is implemented into each control point *A*. Then the NURBS functions can be defined as

$$R_A(\xi,\eta)=\frac{N_A\zeta_A}{\sum_{A}^{m\times n}N_A(\xi,\eta)\zeta_A} \tag{17}$$

It is clear that B-spline function is recovered when the individual weight of control point ζ_A is constant.

3.2. Extended isogeometric finite element method

The basic idea is that enriched functions to capture the local discontinuous and singular fields are enhanced in the standard approximation as follow [37]:

$$\mathbf{u}^h(\mathbf{x})=\sum_{I\in S}N_I(\mathbf{x})\mathbf{q}_I^{std}\ +\ enrichment\ fields \tag{18}$$

where $N_I(\mathbf{x})$ and $\mathbf{q}_I^{std}=\left[u_{0I}\ v_{0I}\ w_{0I}\ \beta_{xI}\ \beta_{yI}\right]^T$ are the standard finite element shape function and nodal degrees of freedom associated with node *I*. To enhance the capability of IGA in analyzing cracked structures, a new numerical procedure – so-called eXtended IsoGeometric Analysis (XIGA) was presented by Luycker et al. [48], Ghorashi et al. [38], Nguyen et al. [49] as combination of IGA

and PUM. Being different from XFEM which uses the Lagrange polynomials in approximation, XIGA utilizes the NURBS basis functions

$$\mathbf{u}^h(\mathbf{x}) = \sum_{I \in S} R_I(\boldsymbol{\xi}) \mathbf{q}_I^{std} + \sum_{J \in S^{enr}} R_J^{enr}(\boldsymbol{\xi}) \mathbf{q}_J^{enr} \tag{19}$$

in which R_J^{enr} are the enrichment functions associated with node J located in enriched domain S^{enr} which is split up two parts including: a set S^c for Heaviside enriched control points and a set S^f for crack tip enriched control points as shown in Figure 5. Furthermore, the enriched functions determined specifically for each domain will be shown next.

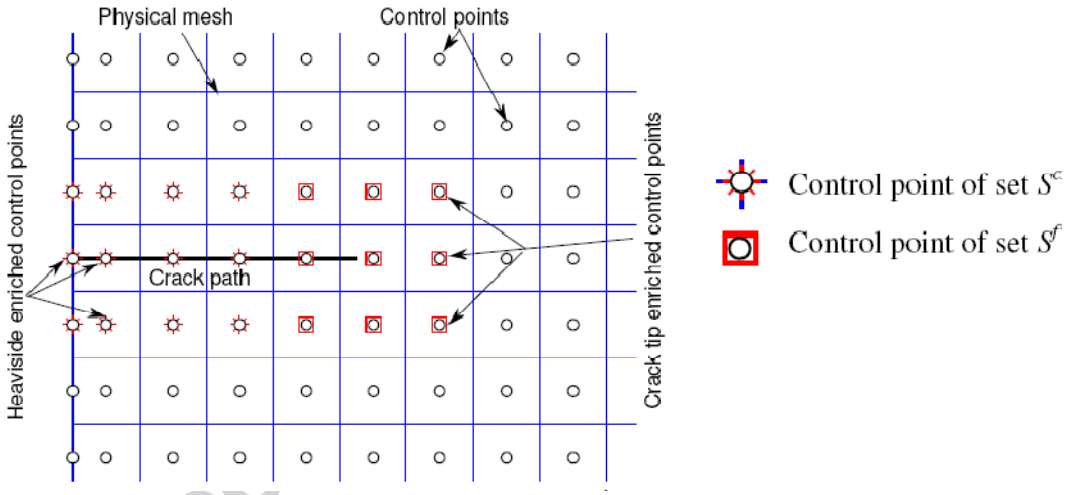

Figure 5. Illustration of the nodal sets S^c, S^f for a quadratic NURBS mesh.

3.3. Cracked plate formulation based on HSDT

To describe the discontinuous displacement field, the enrichment function is given by

$$R_J^{enr}(\boldsymbol{\xi}) = R_J(\boldsymbol{\xi})\big(H(\mathbf{x}) - H(\mathbf{x}_J)\big), \quad J \in S^c \tag{20}$$

where the Heaviside function is defined as

$$H(\mathbf{x}) = \begin{cases} +1 & \text{if } (\mathbf{x}-\mathbf{x}^*)\mathbf{n} > 0 \\ -1 & \text{orthewise} \end{cases} \tag{21}$$

in which **x*** is projection of point **x** on the crack path, and **n** is the normal vector of crack at point **x***. Because the Heaviside function is a step function, its derivative equals to zero [27, [38, [40]. Thus, the first derivative of Heaviside enrichment function is in the following form

$$\begin{aligned} (R_J^{enr})' &= \left[R_J \left(H(\mathbf{x}) - H(\mathbf{x}_J) \right) \right]' = R_J' \left(H(\mathbf{x}) - H(\mathbf{x}_J) \right) + R_J \underbrace{\left(H(\mathbf{x}) - H(\mathbf{x}_J) \right)'}_{0} \\ &= R_J' \left(H(\mathbf{x}) - H(\mathbf{x}_J) \right) \end{aligned} \tag{22}$$

Similarly, the second derivative of Heaviside enrichment function is expressed as

$$\begin{aligned} (R_J^{enr})'' &= \left[R_J' \left(H(\mathbf{x}) - H(\mathbf{x}_J) \right) \right]' = R_J'' \left(H(\mathbf{x}) - H(\mathbf{x}_J) \right) + R_J' \underbrace{\left(H(\mathbf{x}) - H(\mathbf{x}_J) \right)'}_{0} \\ &= R_J'' \left(H(\mathbf{x}) - H(\mathbf{x}_J) \right) \end{aligned} \tag{23}$$

Let consider the one-dimensional domain discretized into three elements as illustrated in Figure 6. For an open uniform knot vector $\Xi = [0\ 0\ 0\ 0\ 1/3\ \ 2/3\ \ 1\ 1\ 1\ 1]$, the cubic B-spline basic functions and their first derivatives are revealed in Figure 6b and c, respectively. It is clearly observed that the C^2 and C^1 continuities are gained at all interior knots for basis functions and their derivatives, respectively. As compute the discontinuity at position $\xi = 0.45$ of the second element, the Heaviside enriched functions in Eq. (20) are used. By multiplying with the step function, they gain the opposite values through the crack point. That enables us to model the discontinuity. As seen in Figure 6d and e, the Heaviside enrichment functions and their first derivatives also keep the original continuities except the crack position. On the other hand, the tip enrichment function can be written by the following form [50]:

$$R_J^{enr}(\xi) = R_J(\xi) \left(\sum_{L=1}^{4} \left(G_L(r,\theta) - G_L(r_J,\theta_J) \right) \right), \quad J \in S^f \tag{24}$$

where

$$G_L(r,\theta)=\begin{cases} r^{3/2}\left[\sin\frac{\theta}{2} \quad \cos\frac{\theta}{2} \quad \sin\frac{3\theta}{2} \quad \cos\frac{3\theta}{2}\right] & \text{for } \mathbf{u}_1 \text{ variable} \\ r^{1/2}\left[\sin\frac{\theta}{2} \quad \cos\frac{\theta}{2} \quad \sin\frac{\theta}{2}\sin\theta \quad \cos\frac{\theta}{2}\sin\theta\right] & \text{for } \boldsymbol{\beta} \text{ variable} \end{cases} \tag{25}$$

in which r and θ are polar coordinates in the local crack tip coordinate system.

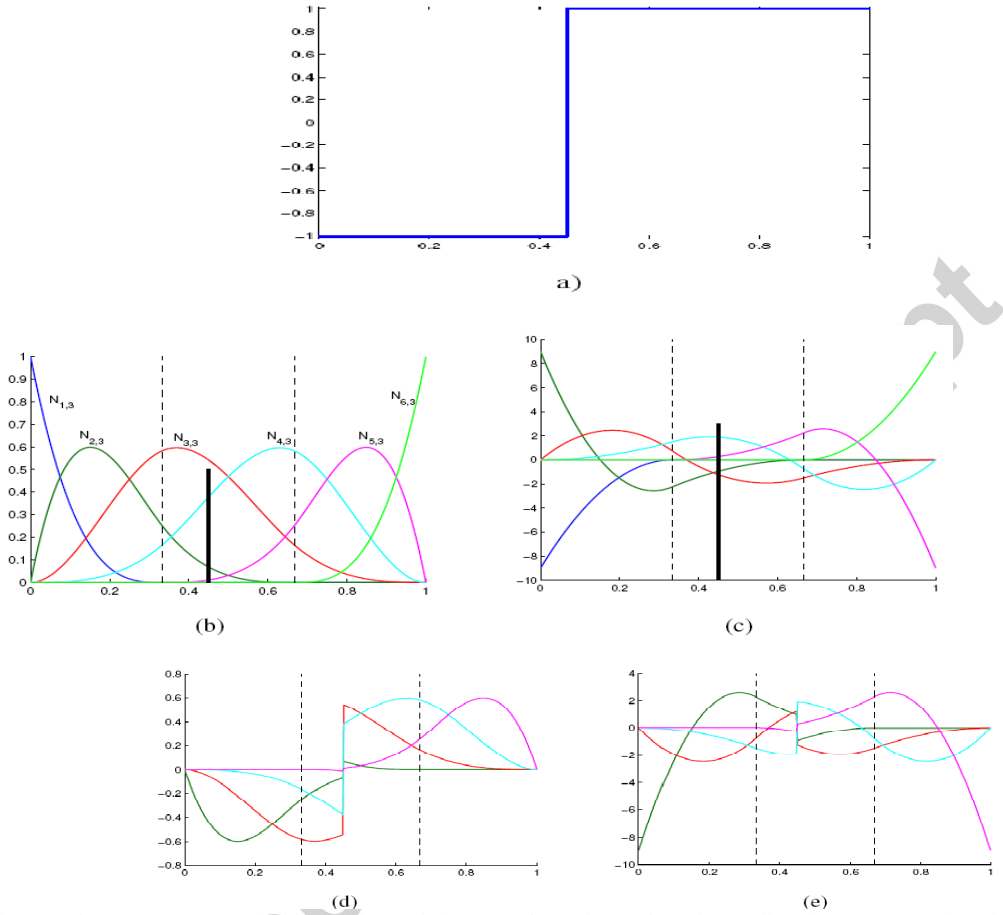

Figure 6: An 1D example of the enrichment functions for the split element cut by the crack: (a) The Heaviside function; (b) the B-spline basis functions and (c) their first derivative; the support domain in a discontinuous position $\xi = 0.45$: (d) the enrichment functions and (e) their first derivative.

Now, substituting the displacement field approximated in Eq. (19) into Eq. (8) the strain matrices including in-plane and shear strains can be rewritten as:

$$\left[\boldsymbol{\varepsilon}_0^T \ \boldsymbol{\kappa}_1^T \ \boldsymbol{\kappa}_2^T \ \boldsymbol{\varepsilon}_s^T\right]^T = \sum_{I=1}^{m\times n}\left[\left(\mathbf{B}_I^m\right)^T \ \left(\mathbf{B}_I^{b1}\right)^T \ \left(\mathbf{B}_I^{b2}\right)^T \ \left(\mathbf{B}_I^s\right)^T\right]^T \mathbf{q}_I \tag{26}$$

in which the unknown vector $\mathbf{q}$ contains both displacements and enriched DOFs, and

$$\mathbf{B} = \left[\mathbf{B}^{std} \middle| \mathbf{B}^{enr} \right] \tag{27}$$

where $\mathbf{B}^{std}$ and $\mathbf{B}^{enr}$ are the standard and enriched strain matrices of $\mathbf{B}$ defined in the following forms:

$$\begin{aligned}
\mathbf{B}^{m} &= \begin{bmatrix} \bar{R}_{,x} & 0 & 0 & 0 & 0 \\ 0 & \bar{R}_{,y} & 0 & 0 & 0 \\ \bar{R}_{,y} & \bar{R}_{,x} & 0 & 0 & 0 \end{bmatrix}, \quad \mathbf{B}^{b1} = -\begin{bmatrix} 0 & 0 & \bar{R}_{,xx} & 0 & 0 \\ 0 & 0 & \bar{R}_{,yy} & 0 & 0 \\ 0 & 0 & 2\bar{R}_{,xy} & 0 & 0 \end{bmatrix}, \\
\mathbf{B}^{b2} &= \begin{bmatrix} 0 & 0 & 0 & \bar{R}_{,x} & 0 \\ 0 & 0 & 0 & 0 & \bar{R}_{,y} \\ 0 & 0 & 0 & \bar{R}_{,y} & \bar{R}_{,x} \end{bmatrix}, \qquad \mathbf{B}^{s} = \begin{bmatrix} 0 & 0 & 0 & \bar{R} & 0 \\ 0 & 0 & 0 & 0 & \bar{R} \end{bmatrix}
\end{aligned} \tag{28}$$

where $\bar{R}$ can be either the NURBS basic functions $R(\boldsymbol{\xi})$ or enriched functions R^{enr}.

Substituting Eq. (7) with relation in Eq. (26) into Eq. (9), the formulations of free vibration problem can be rewritten as follow:

$$\left(\mathbf{K} - \omega^2 \mathbf{M}\right)\mathbf{d} = \mathbf{0} \tag{29}$$

where $\omega \in \mathbb{R}^{+}$ are the natural frequency and the global stiffness matrix $\mathbf{K}$ is given by:

$$\mathbf{K} = \int_{\Omega} \left[\left\{ \mathbf{B}^{m} \;\; \mathbf{B}^{b1} \;\; \mathbf{B}^{b2} \right\} \mathbf{D}^{b} \left\{ \mathbf{B}^{m} \;\; \mathbf{B}^{b1} \;\; \mathbf{B}^{b2} \right\}^{T} + \mathbf{B}^{sT} \mathbf{D}^{s} \mathbf{B}^{s} \right] \mathrm{d}\Omega \tag{30}$$

The global mass matrix $\mathbf{M}$ is expressed as:

$$\mathbf{M} = \int_{\Omega} \tilde{\mathbf{N}}^{T} \mathbf{m} \tilde{\mathbf{N}} \mathrm{d}\Omega \tag{31}$$

in which

$$\begin{aligned}
\tilde{\mathbf{N}} &= \begin{Bmatrix} \mathbf{N}_1 \\ \mathbf{N}_2 \\ \mathbf{N}_3 \end{Bmatrix}, \qquad \mathbf{N}_1 = \begin{bmatrix} \bar{R} & 0 & 0 & 0 & 0 \\ 0 & \bar{R} & 0 & 0 & 0 \\ 0 & 0 & \bar{R} & 0 & 0 \end{bmatrix}; \\
\mathbf{N}_2 &= -\begin{bmatrix} 0 & 0 & \bar{R}_{,x} & 0 & 0 \\ 0 & 0 & \bar{R}_{,y} & 0 & 0 \\ 0 & 0 & 0 & 0 & 0 \end{bmatrix}; \quad \mathbf{N}_3 = \begin{bmatrix} 0 & 0 & 0 & \bar{R} & 0 \\ 0 & 0 & 0 & 0 & \bar{R} \\ 0 & 0 & 0 & 0 & 0 \end{bmatrix}
\end{aligned} \tag{32}$$

It is observed from Eq. (30) that the shear correction factors are no longer required in the stiffness formulation. Furthermore, it is seen that $\mathbf{B}^{b1}$ contains the second-order derivative of the shape function. Hence, it requires C^1-continuous approximation across inter-element boundaries in the finite element mesh. This is not a very trivial task in standard finite element method. In attempts to address this difficulty, several C^0 continuous elements [52-54] were then proposed. Alternatively, Hermite interpolation function with the C^1-continuity was added to satisfy specific approximation of transverse displacement [55]. They may produce extra unknown variables leading to an increase in the computational cost. It is now interesting to note that our present formulation based on NURBS basic functions satisfies naturally continuous condition from the theoretical/mechanical viewpoint of FGM plates [56,57]. In our work, the basic functions are C^{p-1} continuous. As a result, as $p \geq 2$, the present approach ensures C^1-requirement in approximate formulations based on the higher order shear deformation theory.

4. Results and discussions

In this section, we study the natural frequency of the FGM plates with two kinds of crack: a center crack and an edge crack. Herein, ceramic-metal functionally graded plates of which material properties given in Table 1 are considered. We exploit cubic basis functions for almost numerical examples, except a circular plate problem that quadratic basis functions are also used. Herein, present method employes a full integration of $(p+1)\times(q+1)$ Gauss points for the standard elemtents and a subtriangles technique [38] for the enriched elements. The results, unless specified otherwise, are normalized as

$$\bar{\omega} = \omega L^2 / h\sqrt{\rho_c / E_c} \tag{33}$$

Table 1: Material property.

	Al	ZrO_2	Al_2O_3
E (GPa)	70	200	380
ν	0.3	0.3	0.3

ρ (kg/m^3)	2707	5700	3800

4.1. Center crack plate

Let us consider an isotropic plate with dimension $L \times W \times h$ having a center crack length a as shown in Figure 7a. The plate having fully simply supported is discretizing in 21x21 cubic elements as plotted in Figure 7b. Firstly, the relation between the first five natural frequencies and the length-to-thickness ratio *L/h* of an intact plate is shown in Figure 8. Herein, increase in *L/h* ratio makes the obtained natural frequencies from the thick plate theories such as: FSDT and TSDT increase accordingly and converge to CPT results by Leissa [51]. While the TSDT (Figure 8(b)) produces the well matched results with thin plate frequencies, a significant decrease in accuracy is observed from the FSDT (Figure 8(a)) for extremely thin plate (*L/h*>1000). The phenomenon may be attributed to the shear-locking of the FSDT plate model for very thin plates. As seen, with the ratio *L/h*=100, the present model gains consistent values as compared to the thin plate theory within less than 0.5% of error. As take into account the crack, Table 2 reveals the effect of *L/h* ratio on the first five natural frequencies $\hat{\omega} = \omega L^2 \sqrt{\rho h / D}$ of a center crack plate (*a/L*=0.5), where $D = Eh^3 / \left(12(1-\nu^2)\right)$ is the flexural rigidity of the plate. As expected, the obtained results match well with 3D solutions using Ritz method by Huang [34]. Herein, the same observation is that increase in the length-to-thickness ratio makes the plates become thinner and the results reach to CPT solutions by Stahl and Keer [17] and Liew [25]. In case of very thin plate (*L/h*=100), the present model using thick plate theory also yields highly consistent results with lower than 1% error. Thus, for comparison with thin plate results, the length-to-thickness ratio *L/h*=100 is used for computing.

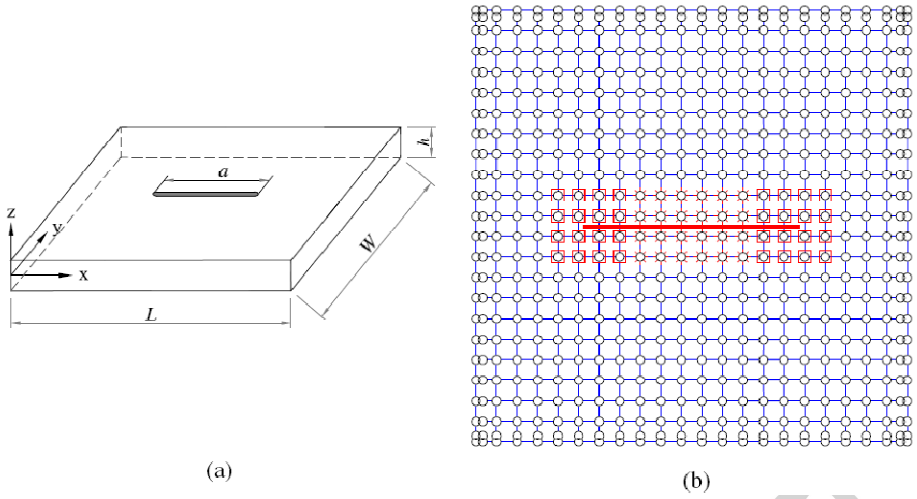

Figure 7. The plate with a center crack: (a) model; (b) a mesh of 21x21 cubic B-spline elements.

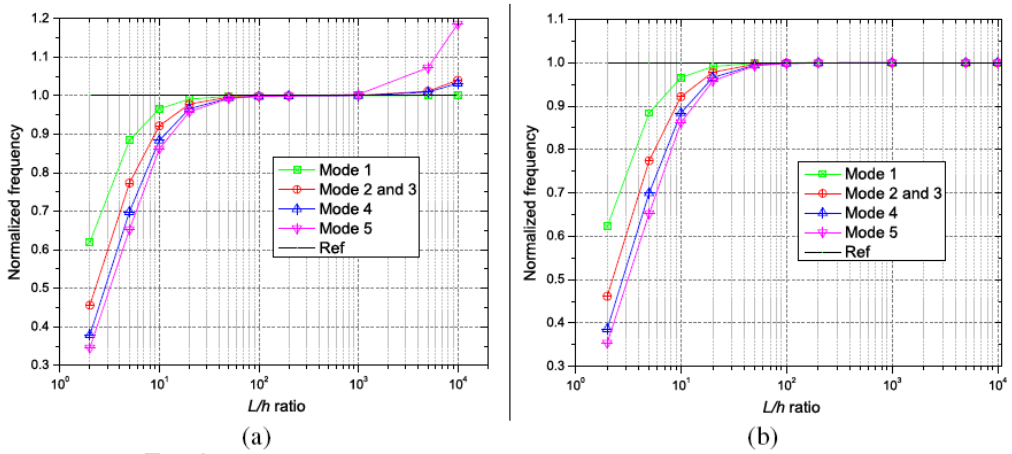

Figure 8. The natural frequency of intact plate via length to thickness ratio: (a) FSDT and (b) TSDT.

Table 2: Effect of *L/h* ratio on the non-dimension frequency $\hat{\omega}$ of the center cracked plate (*a/L*=0.5).

L/h	source	Mode 1	Mode 2	Mode 3	Mode 4	Mode 5
5	3D elasticity [34]	15.3099	28.9610	37.7709	52.7735	55.8137
	XIGA (TSDT)	15.2563	29.8746	37.3251	52.4719	55.3396
	XIGA (FSDT)	15.2478	28.9675	37.4698	52.3002	55.3078
10	3D elasticity [34]	16.7507	36.6804	44.7765	67.2474	70.8494
	XIGA (TSDT)	16.7205	37.2500	44.4276	66.8942	70.3951
	XIGA (FSDT)	16.7155	36.8069	44.6413	67.0764	70.5312
20	3D elasticity [34]	17.3092	40.5798	47.4863	74.1539	77.9872
	XIGA (TSDT)	17.2894	40.9878	47.2903	73.9589	77.6872
	XIGA (FSDT)	17.2810	40.7329	47.4410	74.1472	77.8016
100	3D elasticity [34]	17.6892	42.8930	48.6429	77.5246	81.9196
	XIGA (TSDT)	17.6638	43.3424	48.5695	77.4614	81.7008
	XIGA (FSDT)	17.6595	43.6574	48.6100	77.5809	81.7446
CPT	Stahl [17]	17.706	43.031	48.697	77.733	82.155
	Liew [25]	17.85	42.82	48.72	77.44	83.01

Next, Table 3 tabulates a convergence study of the first five natural frequencies $\hat{\omega}$ of the thin plate. It is observed that within thick plate theories such as FSDT and TSDT, present method gains good accuracy with slight lower results as compared to that of CPT [17, 25] with very small errors less than 0.18% for the intact plate and 0.96% for the crack one, respectively. Using mesh of 21x21 cubic elements, the relation between non-dimension frequencies $\hat{\omega}$ and crack length ratio is reported in Table 4. The results obtained from XIGA are in good agreement with those CPT solution by Stahl [17] using Levy-Nadia approach, Liew et al. [25] using the domain decomposition method, that of 3D

elasticity [34] and Mindlin plate theory [58] using Ritz method. In addition, the comparison of first five frequencies with CPT results is depicted in Figure 9. It reveals that the frequencies decrease via increase in crack length ratio. For example, the values of frequency according to change of mode from 1 to 5 drop up to 18.4%, 67.3%, 5.4%, 40.8% and 23.8% of its initial values corresponding to an intact plate, respectively. It is concluded that the magnitude of the frequency according to anti-symmetric modes through the *y*-axis, which is perpendicular to the cracked path (e.g. mode 2, mode 4, as shown in Figure 10), is much more affected by the crack length. The discontinuous displacement is shown clearly along the crack path.

Table 3: Convergence study of natural frequencies for the thin plate.

a/L	Mode	TSDT					FSDT	Stahl	Leissa
	number	9x9	13x13	17x17	21x21	25x25	25x25	[17]	[51]
0	1	19.7321	19.7320	19.7320	19.7320	19.7320	19.7320	19.739	19.739
	2	49.3090	49.3044	49.3036	49.3033	49.3033	49.3033	49.348	49.348
	3	49.3090	49.3044	49.3036	49.3033	49.3033	49.3033	49.348	49.348
	4	78.8495	78.8437	78.8426	78.8423	78.8422	78.8422	78.957	78.957
	5	98.6002	98.5341	98.5225	98.5193	98.5181	98.5181	98.696	98.696
0.5	1	17.5193	17.6820	17.6744	17.6638	17.6555	17.6473	17.706	-
	2	40.7297	43.4868	43.4441	43.3424	43.2637	43.4461	43.031	-
	3	45.3888	48.2668	48.5149	48.5695	48.5857	48.6015	48.697	-
	4	66.4784	76.5502	77.3085	77.4614	77.5011	77.5584	77.733	-
	5	69.5361	81.7570	81.7221	81.7008	81.6812	81.6758	82.155	-

Table 4: Non dimensional natural frequency of the isotropic square plate via crack length ratio (*L/h*=100)

Mode shape	Source	Crack length ratio *a/L*						
		0	0.2	0.4	0.5	0.6	0.8	1
1	Stahl [17]	19.739	19.305	18.279	17.706	17.193	16.403	16.127
	Liew [25]	19.74	19.38	18.44	17.85	17.33	16.47	16.13
	Ritz method				17.69(*)	17.13(**)		
	XIGA(TSDT)	19.732 (0.04)	19.2638 (0.21)	18.2349 (0.24)	17.6638 (0.24)	17.1305 (0.36)	16.3587 (0.27)	16.1096 (0.11)
	XIGA(FSDT)	19.732 (0.04)	19.2711 (0.18)	18.2324 (0.25)	17.6595 (0.26)	17.1204 (0.42)	16.3544 (0.30)	16.1092 (0.11)
2	Stahl [17]	49.348	49.170	46.624	43.031	37.978	27.773	16.127
	Liew [25]	49.35	49.16	46.44	42.82	37.75	27.43	16.13
	Ritz method				42.89	37.69		
	XIGA (TSDT)	49.3033 (0.09)	49.098 (0.15)	46.7232 (0.21)	43.3424 (0.72)	38.1929 (0.57)	27.9035 (0.47)	16.1096 (0.11)
	XIGA (FSDT)	49.3034 (0.09)	49.1147 (0.11)	46.8296 (0.44)	43.6574 (1.46)	38.3476 (0.97)	28.0654 (1.05)	16.1092 (0.11)
3	Stahl [17]	49.348	49.328	49.032	48.697	48.223	47.256	46.742
	Liew [25]	49.35	49.31	49.04	48.72	48.26	47.27	46.74
	Ritz method				48.64	48.13		
	XIGA (TSDT)	49.3033 (0.09)	49.2557 (0.15)	48.9313 (0.21)	48.5695 (0.26)	48.1013 (0.25)	47.0781 (0.38)	46.6618 (0.17)
	XIGA (FSDT)	49.3034 (0.09)	49.2761 (0.11)	48.9668 (0.13)	48.6100 (0.18)	48.1154 (0.22)	47.088 (0.36)	46.6611 (0.17)

4	Stahl [17]	78.957	78.957	78.602	77.733	75.581	65.732	46.742
	Liew [25]	78.96	78.81	78.39	77.44	75.23	65.19	46.74
	Ritz method				77.52	75.28		
	XIGA (TSDT)	78.8423	78.7275	78.3262	77.4614	75.4169	65.7993	46.6618
		(0.15)	(0.29)	(0.35)	(0.35)	(0.22)	(0.10)	(0.17)
	XIGA (FSDT)	78.8424	78.7689	78.4028	77.5809	75.4895	65.9949	46.6611
		(0.15)	(0.24)	(0.25)	(0.20)	(0.12)	(0.40)	(0.17)
5	Stahl [17]	98.696	93.959	85.510	82.155	79.588	76.371	75.285
	Liew [25]	98.70	94.69	86.71	83.01	80.32	76.60	75.28
	Ritz method				81.92	79.22		
	XIGA (TSDT)	98.5193	92.9166	84.9408	81.7008	79.2038	76.0646	75.1033
		(0.18)	(1.11)	(0.67)	(0.55)	(0.48)	(0.40)	(0.24)
	XIGA (FSDT)	98.5206	93.4560	85.0508	81.7446	79.1787	76.0581	75.1019
		(0.18)	(0.54)	(0.54)	(0.50)	(0.51)	(0.41)	(0.24)

(*)3D-elasticity theory [34], and (**)Mindlin plate theory [58]

The relative errors compared with CPT's solution [17] are shown in parenthesis.

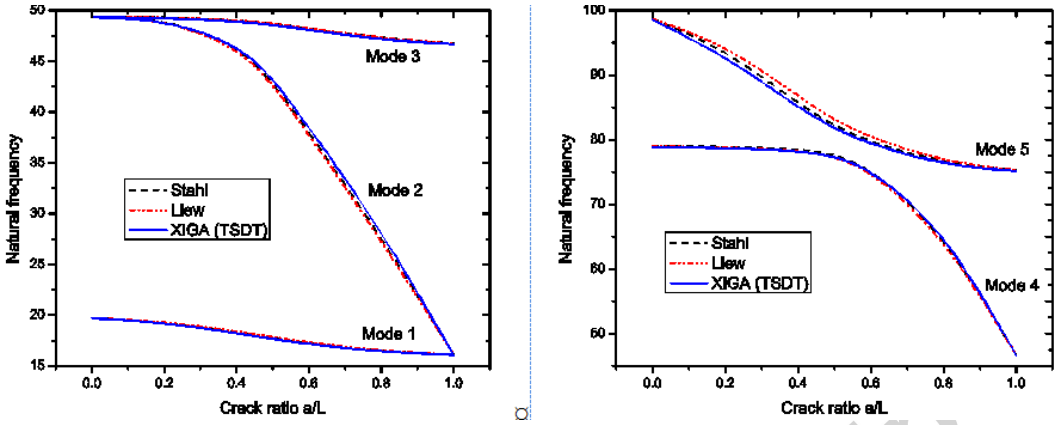

Figure 9. Variation of first five mode frequencies via crack length ratios.

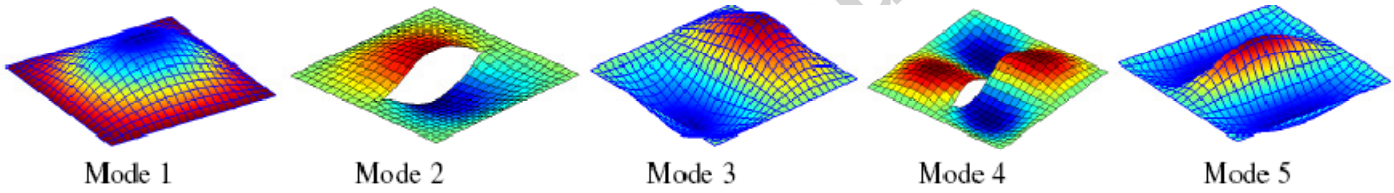

Figure 10. The first five mode shapes of the simply supported plate with the center crack with a/L =0.8

Finally, the effect of length to thickness ratio L/h on the frequencies of Al/Al_2O_3 FGM plate is shown in Figure 11. In this example, the material properties are calculated by two homogenization schemes including the rule of mixture and the Mori-Tanaka scheme with the power index $n = 1$ according to Eqs. (2) and (4). For inhomogeneous materials, the effective property through the thickness of the former is higher than the latter one. The results from the Mori-Tanaka scheme hence are lower than that of the counterpart because of lower stiffness. Moreover, the value of natural frequency changes rapidly between thick plate (L/h =2) and moderate thin plate (L/h =50) with discrepancy up to 57.2% and 71.3% via the rule of mixture and the Mori-Tanaka scheme, respectively. However, for thin plates (L/h≥100), it is independent on the length to thickness ratio with approximated difference up to 1% due to naturally shear-locking free by the present plate theory.

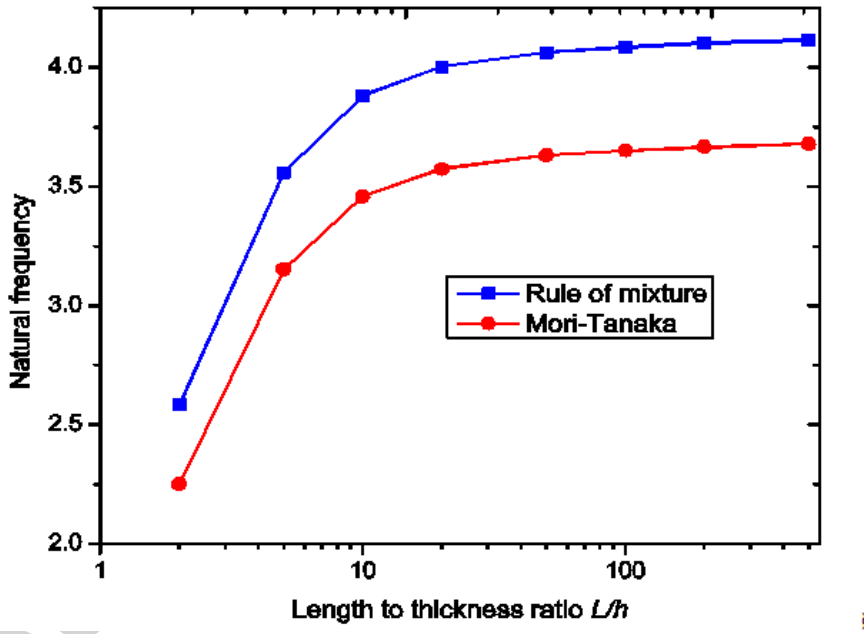

Figure 11. The first frequency of the central cracked Al/Al_2O_3 plate obtained for both mixture and Mori-Tanaka schemes.

4.2. Edge cracked plate

Let us consider a square plate with uniform thickness h and length L, respectively. The FGM plates containing a crack side from the left edge with length a, is discretized into 21x21 cubic NURBS elements as shown in Figure 12. Herein, the variation of material properties through the plate

thickness is evaluated as the rule of mixture given by Eq. (2). Table 5 depicts the effect of the power index n on the first five natural frequencies of a simply supported Al/Al_2O_3 plate with length to thickness ratio L/h=10 and crack length ratio a/L=0.5. The present method gives good agreement compared to both the Ritz method and XFEM. It can be seen that present results are slightly lower than that of Huang et al. [32] based on TSDT or even Natarajan et al. [28] based on FSDT. As compared to 3D elasticity solution calculated by ABAQUS finite element package (resulting in 130791 nodes) [32], the proposed approach based on TSDT model obtains the most accurate first frequency. As shown in Figure 2, increasing volume fraction exponent n reduces the effective property of the material through the plate thickness. Thus, frequency parameter $\bar{\omega}$ decreases respectively because of reduction the stiffness of FGM plate. The same conclusions are drawn for cantilever Al/ZrO_2 cracked plate with results listed in Table 6. The first four mode shapes of the edge cracked FGM plate under fully simply supported and clamped edge right conditions are displayed in **Error! Reference source not found.** and **Error! Reference source not found.**, respectively. It can be seen that the magnitude of deflection based on anti-symmetric mode through the y-axis changes drastically around the crack path (for example, mode 2 and 4).

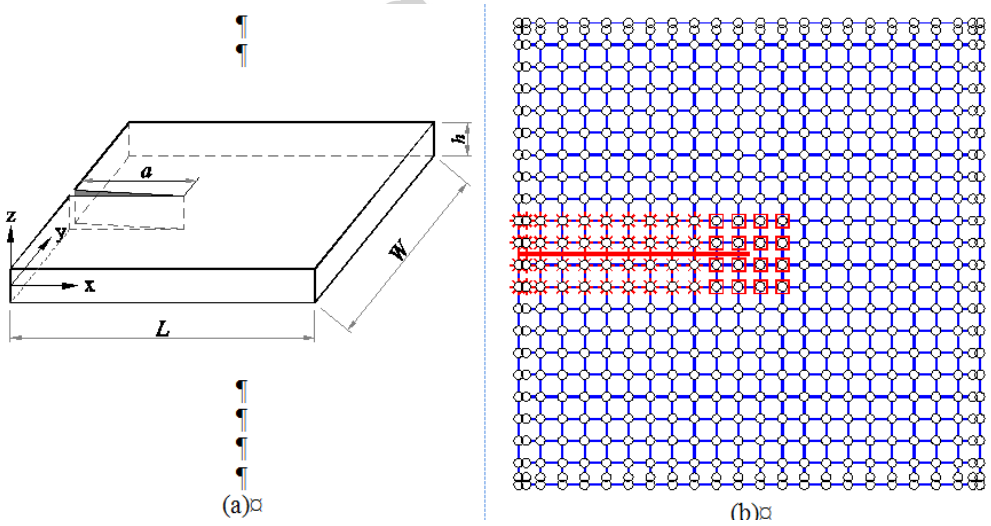

Figure 12. The plate with an edge crack: (a) model; (b) mesh of 21x21 cubic NURBS elements.

Table 5: The first five frequencies of the simply supported Al/Al_2O_3 plate (a/L=0.5)

n	Method	Mode number				
		1	2	3	4	5
0	Ritz method [32]	5.379	11.450	13.320	16.180	17.320
	XFEM [28]	5.387	11.419	13.359	-	-
	XIGA (TSDT)	5.3643	11.4734	13.2801	16.2062	17.2927
	XIGA (FSDT)	5.3657	11.3901	13.2818	16.2062	17.2433
0.2	Ritz method [32]	5.001	10.680	12.410	15.420	16.150
	XFEM [28]	5.028	10.659	12.437	-	-
	XIGA (TSDT)	4.9879	10.7069	12.3702	15.4377	16.1267
	XIGA (FSDT)	4.9877	10.6208	12.3641	15.4376	16.0678
1	3D elasticity [32]	4.115	8.836	10.240	13.330	13.520
	Ritz method [32]	4.122	8.856	10.250	13.310	13.490
	XFEM [28]	4.1220	8.5260	10.2850	-	-
	XIGA (TSDT)	4.1119	8.8791	10.2131	13.3103	13.4946
	XIGA (FSDT)	4.1123	8.8129	10.2139	13.2728	13.4911
5	Ritz method [32]	3.511	7.379	8.621	10.490	11.170
	XFEM [28]	3.626	7.415	8.566	-	-
	XIGA (TSDT)	3.5018	7.3980	8.5912	10.4928	11.1511
	XIGA (FSDT)	3.5218	7.4559	8.6873	10.4956	11.2728
10	Ritz method [32]	3.388	7.062	8.289	9.569	10.710
	XFEM [28]	3.409	7.059	8.221	-	-

XIGA (TSDT)	3.3773	7.0792	8.2582	9.5750	10.6887
XIGA (FSDT)	3.3986	7.1420	8.3594	9.5757	10.8206

Table 6: The first five frequencies of the cantilever Al/ZrO_2 plate (a/L=0.5)

Mode	Method	n				
		0	0.2	1	5	10
1	Ritz method [32]	1.0380	1.0080	0.9549	0.9743	0.9722
	XFEM [28]	1.0380	1.0075	0.9546	0.9748	0.9722
	XIGA (TSDT)	1.0381	1.0076	0.9547	0.9738	0.9716
	XIGA (FSDT)	1.0380	1.0074	0.9546	0.9744	0.9721
2	Ritz method [32]	1.7330	1.6840	1.5970	1.6210	1.6170
	XFEM [28]	1.7329	1.6834	1.5964	1.6242	1.6194
	XIGA (TSDT)	1.7363	1.6871	1.6006	1.6238	1.6189
	XIGA (FSDT)	1.7271	1.6778	1.5919	1.6191	1.6135
3	Ritz method [32]	4.8100	4.6790	4.4410	4.4760	4.4620
	XFEM [28]	4.8231	4.6890	4.4410	4.4955	4.4845
	XIGA (TSDT)	4.8084	4.6782	4.4407	4.4743	4.4586
	XIGA (FSDT)	4.8015	4.6695	4.4340	4.4883	4.4693
4	Ritz method [32]	5.2180	5.0780	4.8200	4.8500	4.8340
	XIGA (TSDT)	5.2332	5.0923	4.8336	4.8626	4.8457
	XIGA (FSDT)	5.2067	5.0644	4.8089	4.8618	4.8409
5	Ritz method [32]	6.1850	6.0250	5.7160	5.5900	5.4780
	XIGA (TSDT)	6.1959	6.0246	5.7148	5.5986	5.4866
	XIGA (FSDT)	6.1950	6.0216	5.7139	5.5987	5.4866

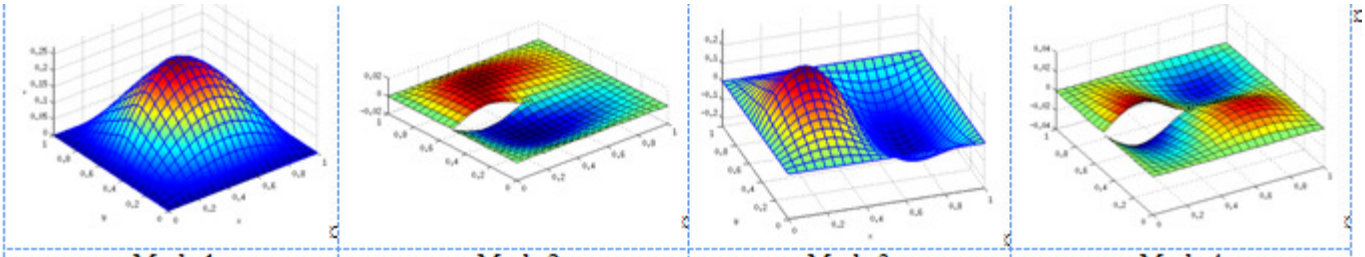

Mode-1 Mode-2 Mode-3 Mode-4

Figure 13. First four mode shapes of the simply supported Al/Al_2O_3 plate with an edge crack.

2 ¶

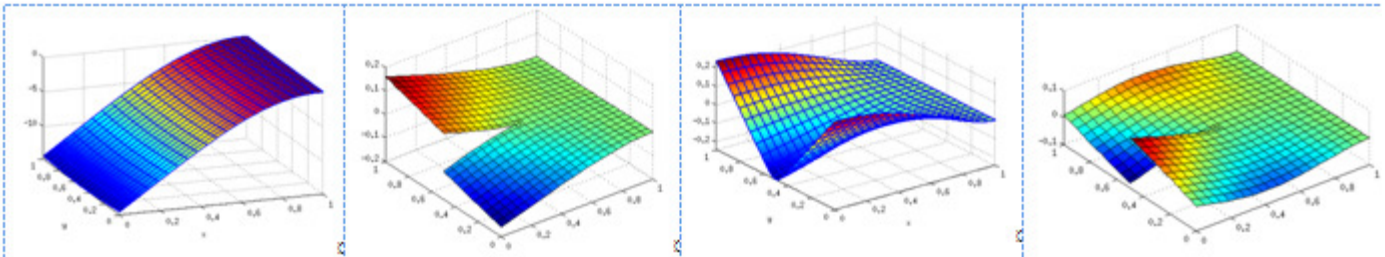

Mode-1 Mode-2 Mode-3 Mode-4

Figure 14. First four mode shapes of the cantilever Al/ZrO_2 plate with the edge crack.

4.3. Circular and annular plates with a center crack

We study circular and annular plates with uniform thickness h, outer radius R and inner one r as shown in Figure 13. The Al/Al_2O_3 FGM plate is clamped at the outer boundary and has a center crack with length $a=(R-r)/2$. Here the Mori-Tanaka homogenization scheme is used.

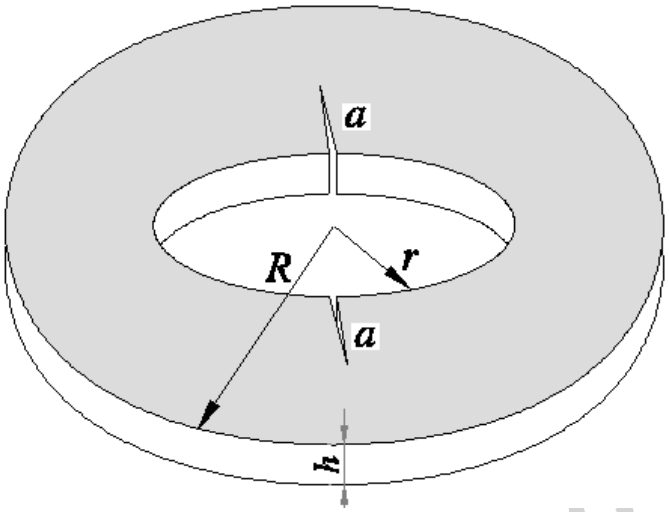

Figure 13. The model of an annular plate.

By setting the inner radius $r = 0$, the geometry model becomes the clamped circular plate with the central crack length $2a$ shown in Figure 14a. The geometry of circular plate is described exactly in Figure 14b with only one quadratic element corresponding to 9 control points which its coordinates are given in Table 7. Note that the value of the individual weight ζ_A associated with these control points is provided to model exactly the curved geometry of the circular plate at the coarsest mesh level.

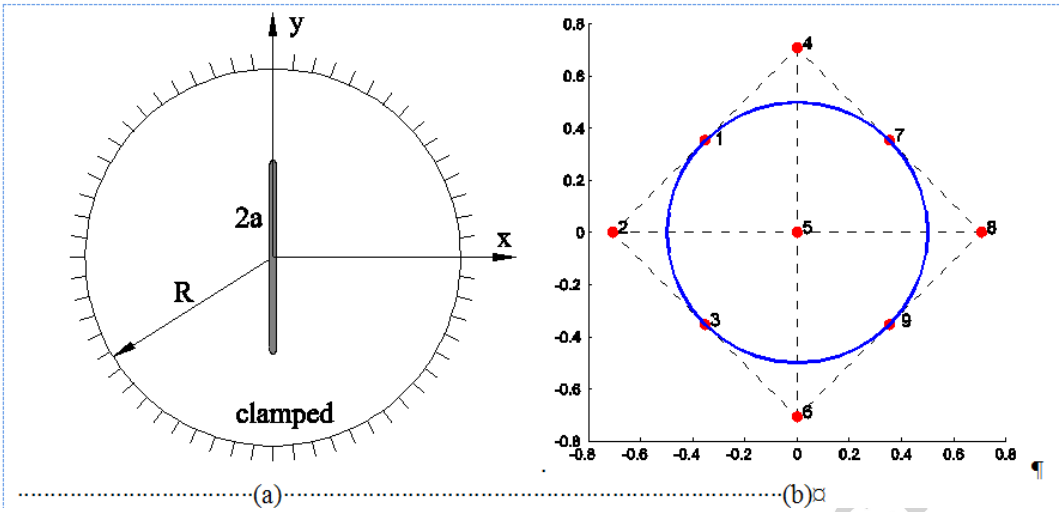

Figure 14. Circular plate: (a) geometry; (b) the coarsest mesh with only one quadratic element.

Table 7: The coordinates and weight values of control points of a circular plate.

Point A	1	2	3	4	5	6	7	8	9
x_A	$-\sqrt{2}/4$	$-\sqrt{2}/2$	$-\sqrt{2}/4$	0	0	0	$\sqrt{2}/4$	$\sqrt{2}/2$	$\sqrt{2}/4$
y_A	$\sqrt{2}/4$	0	$-\sqrt{2}/4$	$\sqrt{2}/2$	0	$-\sqrt{2}/2$	$\sqrt{2}/4$	0	$-\sqrt{2}/4$
ζ_A	1	$\sqrt{2}/2$	1	$\sqrt{2}/2$	1	$\sqrt{2}/2$	1	$\sqrt{2}/2$	1

The reference solution of this problem is not available. The present method is compared relatively with the XFEM [50]. Note that XFEM incorporated with the FSDT employes the selective integration technique in order to enhance the results [18]. The computed frequency parameters $\left(\bar{\omega}=\omega R^2/h\sqrt{\rho_c/E_c}\right)$ are illustrated in Figure 15. Both XFEM and XIGA solutions reduce monotonically when increasing number of degrees of freedom. As expected, the XIGA produces lower frequencies than the XFEM. Table 8 shows the effect of the power index n on the first five natural frequencies. Observation is again that the frequency parameter decreases according to increase in value of n from 0 to 10. It is also seen that there is a bit difference between those elements. It may be caused by: (1) geometric error due to curved geometry is exact description by XIGA based on

NURBS instead of the approximation in XFEM; (2) approximated order: XIGA utilizes NURBS with higher order functions than XFEM using bilinear Lagrange functions. Furthermore, in XIGA, cubic basis functions (p=3) gains less results than quadratic basic functions (p=2). It is believed that with higher order approximated function, cubic elements produce better results. This conclusion has been previously confirmed in [56]. **Error! Reference source not found.** plots the fundamental mode shapes of the circular plate. Using NURBS functions, the curved boundary of the circular plate is still described exactly.

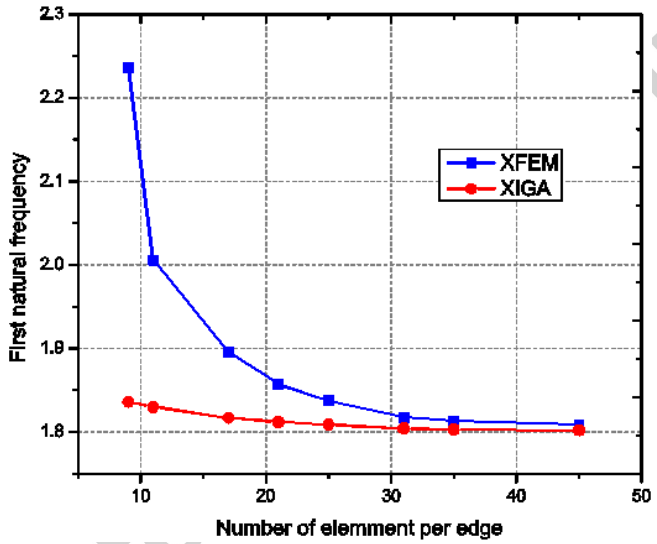

Figure 15. Convergence of the first frequency of a cracked FGM circular plate with $a/R = 0.5$, $h/R = 0.1$, $n = 1$.

Table 8: The first five frequencies $\hat{\omega}$ of a clamped circular Al/Al_2O_3 plate with the central crack (a/R = 0.5)

n	Method	Mode number				
		1	2	3	4	5
0	XFEM(*)	2.6436	4.4598	5.9206	8.6034	9.0733
	XIGA(**) (p=2)	2.6406	4.4929	5.9177	8.6315	9.1287

	XIGA(**) (p=3)	2.6309	4.3435	5.8750	8.5429	8.9441
0.2	XFEM	2.2080	3.7396	4.9485	7.1937	7.5976
	XIGA (p=2)	2.2055	3.7674	4.9467	7.2188	7.6452
	XIGA (p=3)	2.1972	3.6414	4.9111	7.1434	7.4922
1	XFEM	1.8086	3.0674	4.0536	5.8914	6.2259
	XIGA (p=2)	1.8044	3.0869	4.0442	5.8989	6.2474
	XIGA (p=3)	1.7969	2.9762	4.0127	5.8306	6.1146
5	XFEM	1.6364	2.7475	3.6526	5.2942	5.5742
	XIGA (p=2)	1.6288	2.7536	3.629	5.2732	5.5584
	XIGA (p=3)	1.6223	2.6538	3.5999	5.211	5.4347
10	XFEM	1.5678	2.6276	3.4977	5.0687	5.3326
	XIGA (p=2)	1.5624	2.6391	3.4821	5.0609	5.3338
	XIGA (p=3)	1.5564	2.5462	3.4550	5.0036	5.2181

(*)XFEM uses a fine mesh of 45x45 4-node quadrilateral elements;

(**)XIGA uses a mesh of 31x31quadratic (or cubic) NURBS elements.

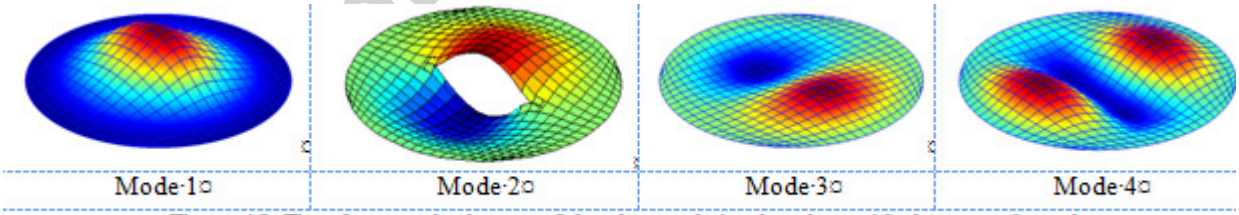

Figure·18.·First·four·mode·shapes·of·the·clamped·circular·plate·with·the·central·crack.¤

Finally, as the inner radius $r \neq 0$ we have the full annular plate shown in Figure 13. Because of symmetry, an upper haft of plate has been modeled in Figure 16 with the symmetric constraint: displacement along y-direction equals to zero at $y = 0$. Based on Eq. (5) the conditions for symmetric boundary are given as

$$v_0 = \beta_y = w_{,y} = 0 \tag{34}$$

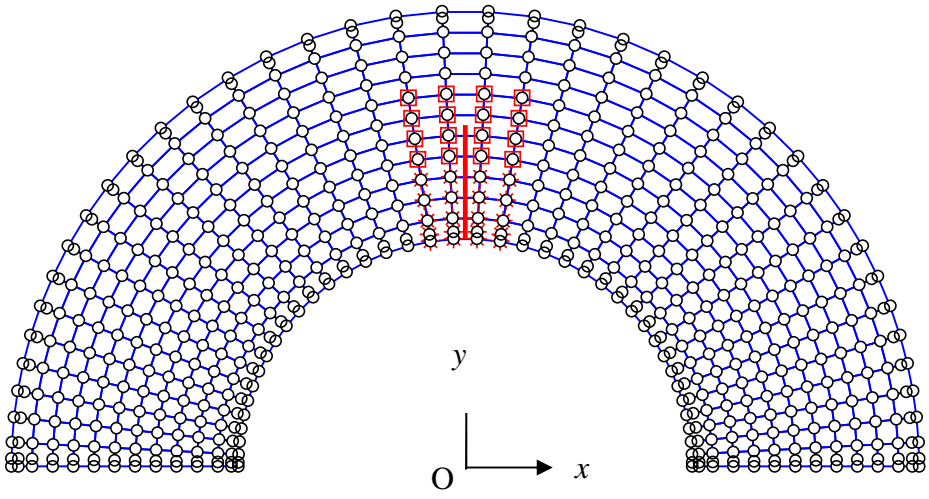

Figure 16. Mesh of an upper half of an annular plate.

The Dirichlet boundary conditions $v_0 = \beta_y = 0$ can be enforced easily. However, the condition $w_{,y} = 0$ can be sufficiently solved by the alternative way [46].

Table 9 shows the frequency parameter of the annular Al/Al_2O_3 plates via outer radius to inner radius ratio *R/r* and radius to thickness ratio *R/h* according to *n*=1. It is concluded that the frequency parameters decrease sequentially by increasing inner radius to outer radius ratio *r/R*. To enclose this section the first four mode shapes of annular FGM plate are depicted in Figure 17.

Table 9: The frequency parameter $\tilde{\omega} = \omega(R-r)^2 / h\sqrt{\rho_c / E_c}$ of the annular pate via inner radius to outer radius ratio *r/R* and radius to thickness ratio *R/h* according to *n* = 1.

R/h	*r/R*	Mode number				
		1	2	3	4	5
2	0	1.2786	1.7682	2.3336	2.7352	2.8058

	0.2	0.8438	1.0109	1.7316	1.8588	1.9021
	0.5	0.5516	0.5896	0.7308	0.8458	0.9817
	0.8	0.2760	0.2771	0.2800	0.2896	0.2905
5	0	1.6804	2.6230	3.5290	4.9598	5.0683
	0.2	1.0877	1.3898	2.7728	3.4371	4.0295
	0.5	0.7845	0.8556	1.1536	1.3664	1.9105
	0.8	0.4923	0.4965	0.5066	0.5225	0.5537
10	0	1.8480	3.5185	4.0473	5.9916	6.3512
	0.2	1.1563	1.5352	3.1932	4.1404	4.8849
	0.5	0.8621	0.9560	1.3533	1.6388	2.3101
	0.8	0.6470	0.6540	0.6730	0.6975	0.7545
20	0	1.8379	3.1941	4.1533	6.1526	6.4956
	0.2	1.1793	1.598	3.3309	4.4139	5.2045
	0.5	0.8877	0.9954	1.4507	1.7937	2.5902
	0.8	0.7279	0.7371	0.7655	0.7999	0.8775
100	0	1.8649	3.3264	4.2398	6.3270	6.7435
	0.2	1.1922	1.6442	3.4202	4.6187	5.3415
	0.5	0.8973	1.0154	1.5007	1.8656	2.6187
	0.8	0.7646	0.7753	0.8124	0.8567	0.9362

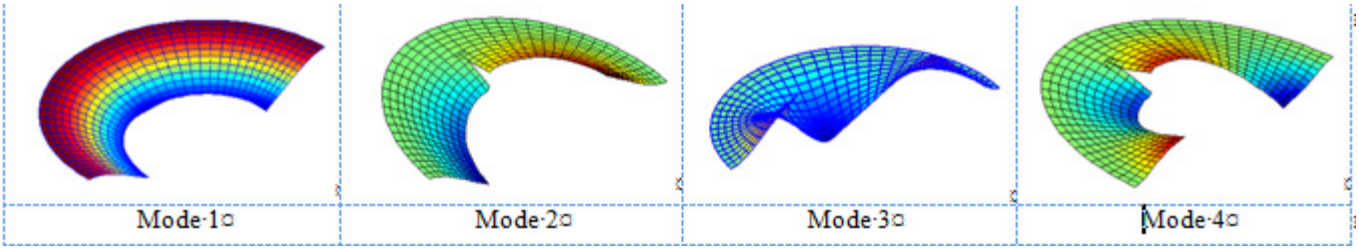

Figure 17. The first four mode shapes of the annular plate with R/r=2, R/h=10.

5. Conclusions

In this paper, a novel and effective formulation based on combining XIGA and HSDT has been applied to dynamic analysis of the cracked FGM plates. The present method utilizing NURBS basis functions allows us to achieve easily the smoothness with arbitrary continuous order compared with the traditional FEM. Consequently, it naturally fulfills the C^1-continuity of HSDT model which is not dependent on dispersed SCF. Furthermore, the special enrichment functions are applied to describe the singularity behaviors of the cracked plates. The obtained results in excellent agreement with that from analytical and numerical methods in the literature demonstrate that XIGA is an effectively computational tool for vibration analysis of the cracked plates.

It is also concluded that magnitudes of the natural frequency decrease via increase in crack length ratio. They change dramatically according to anti-symmetric mode through the y-axis which is perpendicular with crack path.

Herein, two homogenous models based on exponent function of n have been used to estimate the effective property of the FGM plates include the rule of mixture and the Mori-Tanaka technique. It can be seen that, increasing power index n leads to a reduction of frequency parameter of the FGM plates. In addition, to consider the interactions among the constituents, the Mori-Tanaka homogenization scheme gains lower frequency value than the rule of mixture.

Besides, study the benchmarks in rectangular geometry for purpose of comparison, extensive studies was conducted to concentrate in circular and annular FGM plates. It is believed that XIGA with non-geometric approximation can be very promising to provide the good reference results for vibration analysis of these plates with curved boundaries.

Acknowledgements

This research is funded by Vietnam National Foundation for Science and Technology Development (NAFOSTED) under grant number 107.02-2012.17. The support is gratefully acknowledged. The authors would like to acknowledge the Special Funding of Ghent University (Bijzonder Onderzoeksfonds), in the framework of BOF project BOF 01N02410.

References

[1] M. Koizumi, FGM activities in Japan, Composites Part B: Engineering 28 (1997) 1–4.

[2] Y. Fukui, N. Yamanaka, Elastic analysis for thick-walled tubes of functionally graded material subjected to internal pressure, International Journal of Japan Society of Mechanical Engineers Series A 35 (1992) 379–385.

[3] Y. Obata, N. Noda, Transient thermal stresses in a plate of functionally gradient material Ceramic, Tran. Funct. Grad. Mater 34 (1993) 403–410.

[4] J.N. Reddy, Analysis of functionally graded plates, International Journal for Numerical Methods in Engineering 47 (2000) 663–684.

[5] S.V. Senthil, R.C. Batra, Exact solution for thermoelastic deformations of functionally graded thick rectangular plates, AIAA Journal 40 (2002) 1021–1033.

[6] S.V. Senthil, R.C. Batra, Three-dimensional exact solution for the vibration of functionally graded rectangular plates, J Sound. Vib. 272 (2004) 703–730.

[7] J. Yang, H. Shen, Dynamic response of initially stressed functionally graded rectangular thin plates, Compos Struct. 54 (2001) 497–508.

[8] M. Cinefra, E. Carrera, L. Della Croce, C. Chinosi, Refined shell elements for the analysis of functionally graded structures, Composite Structures 94 (2012) 415-422

[9] H. Nguyen-Xuan, Loc V. Tran, T. Nguyen-Thoi, H.C. Vu-Do, Analysis of functionally graded plates using an edge-based smoothed finite element method, Composite Structures 93 (2011) 3019-3039.

[10] H. Nguyen-Xuan, Loc V. Tran, Chien H. Thai, T. Nguyen-Thoi, Analysis of functionally graded plates by an efficient finite element method with node-based strain smoothing, Thin-Walled Structures 54 (2012) 1-18.

[11] Chien H. Thai, S. Kulasegaram, Loc V. Tran, H. Nguyen-Xuan, Generalized shear deformation theory for functionally graded isotropic and sandwich plates based on isogeometric approach, Computers & Structures 141 (2014) 94-112.

[12] H. Nguyen-Xuan, Loc V. Tran, Chien H. Thai, S. Kulasegaramc, S.P.A. Bordas, Isogeometric analysis of functionally graded plates using a refined plate theory, Composites Part B: Engineering 64(2014) 222–234.

[13] A.J.M. Ferreira, R.C. Batra, C.M.C. Roque, L.F. Qian, P.A.L.S. Martins, Static analysis of functionally graded plates using third-order shear deformation theory and a meshless method, Composite Structures 69 (2005) 449–457.

[14] A.J.M. Ferreira, R.C. Batra, C.M.C. Roque, L.F. Qian, R.M.N. Jorge, Natural frequencies of functionally graded plates by a meshless method, Composite Structures 75 (2006) 593–600.

[15] Loc V. Tran, Chien H. Thai, H. Nguyen-Xuan, An isogeometric finite element formulation for thermal buckling analysis of functionally graded plates, Finite Element in Analysis and Design 73 (2013) 65-76.

[16] P. Lynn, N. Kumbasar, Free vibrations of thin rectangular plates having narrow cracks with simply supported edges, Dev. Mech. 4 (1967) 928–991

[17] B. Stahl, L. Keer, Vibration and stability of cracked rectangular plates, Int. J. Solids Struct. 8 (1972) 69–91.

[18] N.S. Putcha, J.N. Reddy, A refined mixed shear flexible finite element for the nonlinear analysis of laminated plates, Computers & Structures 22 (1986) 529-538.

[19] Y. Hirano, K. Okazaki, Vibration of cracked rectangular plates. Bull JSME 23 (1980) 732–740.

[20] GL. Qian, SN. Gu, JS. Jiang, A finite element model of cracked plates and application to vibration problems, Comput. Struct. 39 (1991) 483–487.

[21] M. Krawczuk, Natural vibrations of rectangular plates with a through crack, J Appl Mech 63 (1993) 491–504.

[22] RKL. Su, AYT. Leung, SC. Wong, Vibration of cracked Kirchhoff's plates, Key Eng Mater 145(1998) 167–172.

[23] J. Yuan, SM. Dickinson, The flexural vibration of rectangular plate systems approached by using artificial springs in the Rayleigh–Ritz method, J Sound Vib 159 (1992) 39–55.

[24] HP. Lee, SP. Lim, Vibration of cracked rectangular plates including transverse shear deformation and rotary inertia, Comput Struct 49 (1993) 715–718.

[25] K.M. Liew, K.C. Hung, M.K. Lim, A solution method for analysis of cracked plates under vibration, Engineering Fracture Mechanics 48 (1994) 393–404.

[26] C.S. Huang, A.W. Leissa, Vibration analysis of rectangular plates with side cracks via the Ritz method, J Sound Vib. 323 (2009) 974–88.

[27] M. Bachene, R. Tiberkak, S. Rechak, Vibration analysis of cracked plates using the extended finite element method, Archive of Applied Mechanics 79 (2009) 249-262.

[28] S.Natarajan, P.M. Baiz, S.Bordas, T.Rabczuk, P. Kerfriden, Natural frequencies of cracked functionally graded material plates by the extended finite element method, Composite Structures 93 (2011) 3082–3092

[29] E. Reissner, On the analysis of first and second order shear deformation effects for isotropic elastic plates, ASME J. Appl. Mech. 47 (1980) 959–961.

[30] R.D. Mindlin, Influence of rotatory inertia and shear on flexural motions of isotropic elastic plates, ASME J. Appl. Mech. 73 (1951) 31–38.

[31] A.J.M. Ferreira, L.M.S. Castro and S. Bertoluzza, A high order collocation method for the static and vibration analysis of composite plates using a first-order theory, Compos. Struct. 34 (2003) 627-636.

[32] C.S. Huang, O.G. McGee III, M.J. Chang, Vibrations of cracked rectangular FGM thick plates, Composite Structure 93 (2011) 1747-1764.

[33] J. Yang, Y. Hao, W. Zhang, S. Kitipornchai, Nonlinear dynamic response of afunctionally graded plate with a through-width surface crack. Nonlin. Dynam. 59 (2010) 207–219.

[34] C.S. Huang, P.J. Yang, M.J. Chang, Three-dimensional vibration analyses of functionally graded material rectangular plates with through internal cracks, Composite Structures, 94 (2012) 2764-2776.

[35] T.J.R. Hughes, J.A. Cottrell, and Y. Bazilevs, Isogeometric analysis: CAD, finite elements, NURBS, exact geometry and mesh refinement, Computer Methods in Applied Mechanics and Engineering 194 (2005) 4135–4195.

[36] J.A. Cottrell, A. Reali, Y. Bazilevs, and T.J.R. Hughes, Isogeometric analysis of structural vibrations, Computer Methods in Applied Mechanics and Engineering 195 (2006) 5257–5296.

[37] T. Belytschko, T. Black, Elastic crack growth in finite elements with minimal remeshing, International Journal of Numerical Methods in Engineering 45 (1999) 601-620.

[38] S.S. Ghorashi, N. Valizadeh, and S. Mohammadi, Extended isogeometric analysis for simulation of stationary and propagating cracks, International Journal for Numerical Methods in Engineering 89 (2012) 1069–1101.

[39] H. Nguyen-Xuan, Loc V. Tran, Chien H. Thai, Canh V. Le, Plastic collapse analysis of cracked structures using extended isogeometric elements and second-order cone programming, Theoretical and Applied Fracture Mechanics 72 (2014) 13-27.

[40] N. Nguyen-Thanh, N. Valizadeh, M.N. Nguyen, H. Nguyen-Xuan, X. Zhuang, P. Areias, G. Zi, Y. Bazilevs, L. De Lorenzis, T. Rabczuk, An extended isogeometric thin shell analysis based

on Kirchhoff–Love theory, Computer Methods in Applied Mechanics and Engineering 284 (2015) 265-291.

[41] T. Mori, K. Tanaka, Average stress in matrix and average elastic energy of materials with misfitting inclusions, Acta Metall 21 (1973) 571–574.

[42] L.F. Qian, R.C. Batra, L.M. Chen, Static and dynamic deformations of thick functionally graded elastic plate by using higher-order shear and normal deformable plate theory and meshless local Petrov–Galerkin method, Composites Part B: Engineering 35 (2004) 685–697.

[43] J.N. Reddy, A simple higher-order theory for laminated composite plates, J. Appl. Mech, 51(1984) 745–752.

[44] M. Karama, K.S. Afaq, S. Mistou, Mechanical behavior of laminated composite beam by new multi-layered laminated composite structures model with transverse shear stress continuity, Int. J. Solids and Structures 40 (2003)1525-1546.

[45] H. Arya, R.P. Shimpi, N.K. Naik, A zigzag model for laminated composite beams, Composite Structures 56 (2002) 21-24.

[46] H. Nguyen-Xuan, Chien H. Thai, T. Nguyen-Thoi, Isogeometric finite element analysis of composite sandwich plates using a new higher order shear deformation theory, Composite Part B 55 (2013) 558–574.

[47] Chien H. Thai, A.J.M. Ferreira, S.P.A. Bordas, T. Rabczuk, H. Nguyen-Xuan, Isogeometric analysis of laminated composite and sandwich plates using a new inverse trigonometric shear deformation theory, European Journal of Mechanics-A/Solids 43 (2014) 89-108.

[48] E. De Luycker, D.J. Benson, T. Belytschko, Y. Bazilevs, and M.C. Hsu, X-FEM in isogeometric analysis for linear fracture mechanics, International Journal for Numerical Methods in Engineering 87 (2011) 541–565.

[49] V.P. Nguyen, S.P.A. Bordas. T. Rabczuk, Isogeometric analysis: an overview and computer implementation aspects, Computer Aided Geometric Design, submitted, 2013.

[50] J. Dolbow, N. Moës, T. Belytschko, Modeling fracture in Mindlin–Reissner plates with the extended finite element method, Int. J. Solids Struct. 37 (2000) 7161–7183.

[51] A.W. Leissa, The free vibration of rectangular plates, Journal of Sound and Vibration 31 (1973) 257-293.

[52] Loc V. Tran, T. Nguyen-Thoi, Chien H. Thai, H. Nguyen-Xuan, An edge-based smoothed discrete shear gap method (ES-DSG) using the C^0-type higher-order shear deformation theory for analysis of laminated composite plates, Mechanics of Advanced Materials and Structures (2013) DOI:10.1080/15376494.2012.736055.

[53] C.A. Sankara and N.G.R. Igengar, A C^0 element for free vibration analysis of laminated composite plates, J. Sound and Vib. 191 (1996) 721–738.

[54] T. Kant and K. Swaminathan, Analytical solutions for the static analysis of laminated composite and sandwich plates based on a higher order refined theory, Composite Structures 56 (1996) 329-344.

[55] H.T. Thai, D.H. Choi, Finite element formulation of various four unknown shear deformation theories for functionally graded plates, Finite Elements in Analysis and Design 75 (2013) 50-61.

[56] Chien H. Thai, H. Nguyen-Xuan, N. Nguyen-Thanh, T-H. Le, T.Nguyen-Thoi, T. Rabczuk, Static, free vibration, and buckling analysis of laminated composite Reissner–Mindlin plates using NURBS-based isogeometric approach, Int. J. Numer. Meth. Engng., 91 (2012) 571–603.

[57] Loc V. Tran, A.J.M. Ferreira, H. Nguyen-Xuan, Isogeometric approach for analysis of functionally graded plates using higher-order shear deformation theory, Composite Part B 51 (2013) 368-383.

[58] C.S. Huang, A.W. Leissa, R.S. Li, Accurate vibration analysis of thick cracked rectangular plates, J. Sound and Vibration 330 (2011) 2079–2093.

Highlights

- We analyze free vibration of functionally graded plates containing cracks.
- The method is derived from higher-order shear deformation theory (HSDT) and extended isogeometric analysis (XIGA).
- The proposed formulation fulfills high-continuity generalized displacements.
- Numerical results show excellent performance of the proposed approach.